PB90-104506

Temperature Dependence of Mass Accommodation of SO2 and H2O2 on Aqueous Surfaces

Aerodyne Research, Inc., Billerica, MA

Prepared for:

Environmental Protection Agency, Research Triangle Park, NC

1989

U.S. Department of Commerce
National Technical Information Service
NTIS

TECHNICAL REPORT DATA
(Please read Instructions on the reverse before completing)

1. REPORT NO.	2.	3. PB90-104506
EPA/600/J-89/077		

4. TITLE AND SUBTITLE
THE TEMPERATURE DEPENDENCE OF MASS ACCOMMODATION OF SO_2 AND H_2O_2 ON AQUEOUS SURFACES

5. REPORT DATE

6. PERFORMING ORGANIZATION CODE

7. AUTHOR(S)
Douglas Worsnop, Mark Zahniser and Charles E. Kolb

8. PERFORMING ORGANIZATION REPORT NO.

9. PERFORMING ORGANIZATION NAME AND ADDRESS
Acrodyne Research Inc.
45 Manning Road
Billerica, MA 01821

10. PROGRAM ELEMENT NO.
N104/C/05/05-5055 (FY-89)

11. CONTRACT/GRANT NO.
Cooperative Agreement 812296

12. SPONSORING AGENCY NAME AND ADDRESS
Atmospheric Research & Exposure Assessment Lab
Office of Research and Development
U.S. Environmental Protection Agency
Research Triangle Park, NC 27711

13. TYPE OF REPORT AND PERIOD COVERED

14. SPONSORING AGENCY CODE
EPA 600/09

15. SUPPLEMENTARY NOTES
To be published in J. Physical Chemistry

16. ABSTRACT

The mass accommodation coefficients of SO_2 and H_2O_2 on aqueous surfaces over the temperature range 260 - 292°K are reported. The experimental method used combined a monodisperse train of droplets and a low pressure flow reactor. Uptake rates were determined by measuring changes in trace gas number density as a function of exposed liquid surface area. Results for SO_2 showed an accommodation coefficient of 0.11 ± 0.02 with no significant temperature variation. H_2O_2 showed a strong temperature dependence with an accommodation coefficient of 0.18 ± 0.02.

→ con't on pg 1157

17. KEY WORDS AND DOCUMENT ANALYSIS

a. DESCRIPTORS	b. IDENTIFIERS/OPEN ENDED TERMS	c. COSATI Field/Group

18. DISTRIBUTION STATEMENT	19. SECURITY CLASS *(This Report)*	21. NO. OF PAGES
RELEASE TO PUBLIC	UNCLASSIFIED	15
	20. SECURITY CLASS *(This page)* UNCLASSIFIED	22. PRICE

EPA Form 2220-1 (9-73)

EPA/600/J-89/077

Reprinted from The Journal of Physical Chemistry, 1989, 93, 1159.
Copyright © 1989 by the American Chemical Society and reprinted by permission of the copyright owner.

Temperature Dependence of Mass Accommodation of SO_2 and H_2O_2 on Aqueous Surfaces

Douglas R. Worsnop,* Mark S. Zahniser, Charles E. Kolb,

Aerodyne Research, Inc., 45 Manning Road, Billerica, Massachusetts 01821

James A. Gardner, Lyn R. Watson, Jane M. Van Doren, John T. Jayne, and Paul Davidovits

Department of Chemistry, Boston College, Chestnut Hill, Massachusetts 02167 *(Received: May 12, 1988)*

We report the laboratory determination of the temperature-dependent mass accommodation coefficients of SO_2 and H_2O_2 on aqueous surfaces over the range 260–292 K. Mass accommodation kinetics involve fundamental chemical interactions of liquid surfaces about which little is known. Uptake of SO_2 and H_2O_2 by cloud droplets is believed to be critical to S(IV) oxidation in the troposphere. Our experimental method combines a monodisperse train of droplets (200 μm in diameter) and a low-pressure flow reactor. Uptake rates of trace gases are determined by measuring changes in trace gas number density as a function of exposed liquid surface area. Experiments with systematic variation of water vapor and rare gas partial pressures permit deconvolution of gas diffusion and temperature-dependent mass accommodation. In the case of SO_2, variation of droplet–gas interactions on millisecond time scales resolved pH-dependent saturation effects at the aqueous surface. Results for SO_2 show $\gamma_{273} = 0.11 \pm 0.02$ with no significant temperature variation. H_2O_2 shows a strong temperature dependence consistent with an attractive well depth of at least 26 kJ mol^{-1} with $\gamma_{273} = 0.18 \pm 0.02$. These results are discussed in terms of the different aqueous solubilities of SO_2 and H_2O_2.

Introduction

The heterogeneous accommodation of gaseous molecules into liquids depends on fundamental properties of liquids and their surfaces. Relatively little is known about this process because of difficulties in studying it. From a theoretical standpoint, analysis of the process requires knowledge both of the solvation process in bulk liquids and of liquid surface structure. Experimentally, the primary difficulty lies in preparing well-defined liquid surfaces with constant properties.

On a practical level the mass accommodation process can be the rate-limiting step in heterogeneous mass transfer in clouds or above oceans.[1] For example, SO_2 and H_2O_2 are of interest because of their role in acid rain formation. Modeling studies indicate aqueous oxidation of SO_2 to SO_4^{2-} occurs in cloud droplets, with H_2O_2 implicated as the primary oxidant.[2,3] Knowledge of gas/liquid mass-transfer rates for these species is critical to modeling of this heterogeneous cloud process.

Gas/liquid mass transfer is a convolution of four processes: (1) diffusion of gas molecules to the liquid surface; (2) accommodation of gas molecules on the surface; (3) possible chemical conversion to form a soluble product; (4) liquid-phase diffusion of dissolved molecules or products away from the liquid surface.

Process 2, the accommodation of gas molecules on the liquid surface, can be characterized by the mass accommodation coefficient (γ), which is defined simply as the probability that a molecule in the gas phase will enter into the liquid upon collision with the liquid surface.

The connection of processes 2 and 3 with 4 is strongly dependent on the solubility of the gas in the liquid (expressed by the Henry's law constant). If mass accommodation is faster than liquid diffusion, then the surface becomes saturated in the trace gas, leading to reevaporation of dissolved trace gas, which reduces the net uptake rate. Experimentally, the goal is to kinetically separate these processes, permitting the direct investigation of the surface accommodation process. However, in general the experimentally measured rate of uptake of a gas into a liquid is smaller than the rate corresponding to the actual γ due to limitations of processes 1, 3, and 4. We express observed rates as the probability coefficient γ_{obsd} which represents a lower limit to γ.

Modeling of gas/liquid mass transfer has assumed that steps 1, 3, and 4 can be evaluated from bulk liquid and gas-phase parameters.[4,5] They are then coupled with one heterogeneous parameter, γ, at the interface. Particularly for relatively insoluble gases, this approach begs the question of whether the accommodation process, which may occur in a surface layer only a few angstroms deep, can be separated into accommodation, reaction, and diffusion steps that can be related to kinetics of the bulk liquid. This ambiguity is reflected in the terms used to describe γ, including reactive sticking and sticking coefficients.[6] In the field of solid surfaces, reactive sticking is distinguished from simple thermal accommodation or sticking.[7]

Historically, there has been much uncertainty in the magnitude of mass accommodation coefficients. Reported values for evaporation coefficients for experiments on several pure liquids have gradually approached unity as experimental techniques have improved.[8,9] In fact, Cammenga has stated that experiment and theory point toward a universal value of unity for evaporation and condensation coefficients of a molecule on its own liquid.[9] The primary experimental difficulty has been in maintaining surface cleanliness and eliminating heat-transfer effects on surface temperature.

The data base for mass accommodation coefficients of trace gases on liquid surfaces is much more limited. The largest body of data has been reported for sticking onto sulfuric acid surfaces in a Knudsen cell.[10,11] The results for a series of molecules indicate that γ on H_2SO_4 is small ($<10^{-3}$) at room temperature. This technique is limited to liquid surfaces with low vapor pressure. Tang and Lee have reported a lower limit of 2×10^{-2} for SO_2 accommodation on an aqueous surface.[12] Because their technique

(1) Chameides, W. L. *J. Geophys. Res.* **1984**, *89*, 4739.
(2) Schwartz, S. E. *J. Geophys. Res.* **1984**, *89*, 11589.
(3) Jacob, D. J. *J. Geophys. Res.* **1986**, *91*, 9807.
(4) Schwartz, S. E. In *Chemistry of Multiphase Atmospheric Systems*; NATO ASI Series; Jaeschke, W., Ed.; Springer-Verlag: Berlin, 1986; Vol. G6, 415.
(5) Schwartz, S. E.; Freiberg, J. E. *Atmos. Environ.* **1981**, *15*, 1129.
(6) Mozurkewich, M.; McMurry, P. H.; Gupta, A.; Calvert, J. G. *J. Geophys. Res.* **1986**, *91*, 4163.
(7) Gates, S. M. *Surf. Sci.* **1988**, *85*, 307.
(8) Lednouich, S. L.; Fenn, J. B. *AICHE J.* **1977**, *23*, 454.
(9) Cammenga, H. K. *Current Topics in Materials Science*: Kaldis, E., Ed.; North-Holland: (*Washington, D.C.*) 1980; Vol. 5, p 335.
(10) Baldwin, A. C.; Golden, D. M. *Science* **1979**, *206*, 562. Baldwin, A. C.; Golden, D. M. *J. Geophys. Res.* **1980**, *85*, 2882.
(11) Martin, L. R.; Judeikis, H. S.; Wun, M. *J. Geophys. Res.* **1980**, *85*, 5511.
(12) Tang, I. N.; Lee, J. H. In *The Chemistry of Acid Rain: Sources and Atmospheric Processes*; Johnson, R. W., Gordon, G. E., Eds.; American Chemical Society Symposium Series; American Chemical Society: Washington, D.C.; 1987; p 109. See also: *Atmos. Environ.* **1988**, *22*, 1147.

0022-3654/89/2093-1159$01.50/0 © 1989 American Chemical Society.

NTIS is authorized to reproduce and sell this report. Permission for further

utilizes a large (10 cm) water surface, deconvolution of gas diffusion rates is critical to extracting an absolute value for γ. An experiment by Mozurkewich et al. has measured a $\gamma > 0.2$ for HO_2 radical on 0.1-μm diameter aerosol particles containing 20 M NH_4SO_4.[6] The very small size of the particles eliminates gas-diffusion limitations. Other recent experiments show intriguing heterogeneous chemistry of HNO_3, N_2O_5, $ClONO_2$, and HCl on ice-coated surfaces in flow tubes and Knudsen cells.[13,14] An inherent limitation in these experimental techniques is the long contact time ($\geq$1 s) between the surface and the laboratory atmosphere. This can affect both surface cleanliness and the degree of surface saturation of the trace gas.

We describe here an experimental technique that measures the uptake of trace gas into a fast-moving train of water droplets. The droplets moving at speeds up to 4400 cm s^{-1} provide a continuously renewed aqueous surface. Contact time between droplets and trace gas can be varied between 0.7 and 13 ms. This reduces the potential for surface contamination or saturation and, under appropriate conditions, permits direct observation of time-dependent saturation of the liquid. Use of small droplets ($\leq$200 μm) and operation at low pressure (2–50 Torr) minimize gas-diffusion limitations. Careful control of the ambient water vapor pressure also permits measurement of the temperature dependence of the mass accommodation process.

We have measured mass accommodation coefficients for SO_2 and H_2O_2 on aqueous droplets as a function of temperature from 260 to 292 K. Previously we have reported one measurement for SO_2 at 292 K in a 20-Torr atmosphere.[15] Measurement of SO_2 and H_2O_2 uptake rates over an extended pressure range has permitted the unambiguous deconvolution of gas-phase diffusion rates. Furthermore, for SO_2 we have directly observed the time-dependent saturation of water droplets that is controlled by its aqueous dissociation equilibria.

In what follows we first present a detailed description of the apparatus and the physical basis of the experimental procedure. Then, measured pressure dependence of trace gas uptake is analyzed to separate gas-diffusion and temperature effects. Finally, we discuss the significance of what we believe is the first accurate measurement of the temperature dependence of mass accommodation coefficients on liquid water surfaces. In particular, the contrasting behavior of SO_2 and H_2O_2 is directly related to their differences in aqueous solubility.

Experimental Section

Our experimental technique[15] measures the uptake of trace gas into a uniform train of water droplets generated with a vibrating orifice.[16] Pressurized water is passed through an orifice in a stainless steel plate that is mechanically vibrated by a piezoelectric ceramic. The latter is tuned to a subharmonic of the "natural" droplet breakup frequency (f_o), first derived by Rayleigh:[17]

$$f_o = \frac{v_d}{4.5 d_o}$$

Typical water backing pressure of 6 bar and orifice diameter (d_o) of 60 μm give droplet velocity v_d = 2700 cm s^{-1} and f_o = 100 kHz. The resulting train of droplets maintains well-defined size and spacing over distances up to 40 cm under moderate vacuum (pressure <60 Torr). Two orifice sizes, 22 and 61 μm in diameter, are used to generate droplets 64–270 μm in diameter moving at speeds of 1500–4400 cm s^{-1}. Such a fast-moving droplet train provides a continuously renewed water surface. The time of exposure for an individual droplet to a trace gas can be varied from 1 to 14 ms.

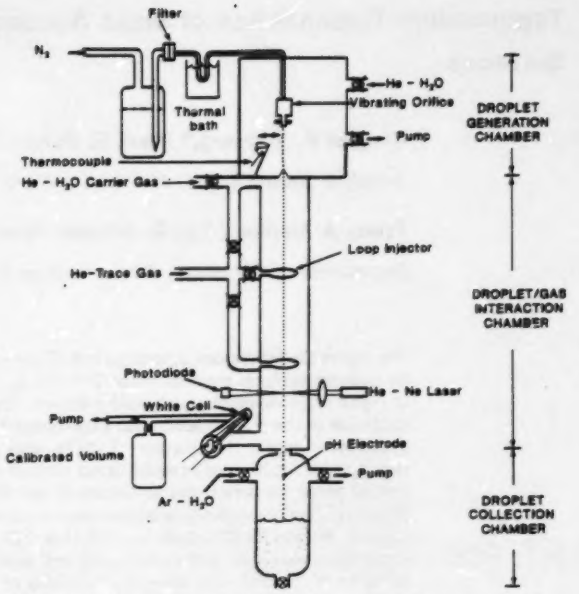

Figure 1. Schematic of coaxial droplet–gas flow apparatus.

Figures 1 and 2 show the two apparatuses that have been constructed to measure trace gas uptake into water droplets. The conceptual design of both is the same: the train of droplets is passed through a flow tube containing a known flow of trace and carrier gases. The droplet generation and collection regions are isolated in separately evacuated chambers so that the droplets comprise the only water surface to which the trace gas is exposed. Tunable diode laser infrared differential absorption is used to measure the concentration of trace gas downstream of the flow tube. The exposed water surface area is varied either by switching the droplet train on and off with a deflector or by switching the droplet frequency, which varies droplet size and spacing. The total pressure and atmospheric composition in each vacuum chamber, as well as the initial temperature of the water stream, are carefully controlled to maintain vapor pressure equilibrium with the water droplets.

In the first apparatus (Figure 1), which has been described previously,[15] the droplet train is passed coaxially down a 20.5-cm flow tube 1.5 cm in diameter. The main carrier gas flow consists of H_2O vapor entrained in a rare gas (He or Ar) passed through a thermostated water bubbler. The water vapor fraction was varied from 20 to 80%. This carrier gas enters and exits through side arms at the top and bottom of the flow tube. Trace gas can be either premixed with the carrier gas entering the top of the flow tube or introduced via Teflon loop injectors in one of two lower side arms. The contact distance of the trace gas with the droplet train is 4, 12, or 20.5 cm for the three different inlets. Depending on the droplet train velocity, this corresponds to droplet–trace gas exposure times of 2–14 ms.

In the second apparatus (Figure 2), the droplet train passes transversely across a 2.7-cm diameter flow tube. Trace and carrier gas flows are injected into the flow tube upstream of the droplet train. This configuration gives droplet–gas exposure times of 0.7–2 ms. The droplet train passes through three separately evacuated chambers before entering the flow tube. The 30-cm distance between orifice and flow tube improves control of the equilibration of the droplets and the ambient atmosphere. This is particularly useful when droplets are supercooled via evaporative cooling before they enter the flow tube. The high conductance of the flow tube also permits operation with the low pressure (<5 Torr) and fast flows (1000 cm s^{-1}) required for study of unstable species such as free radicals.

(13) Molina, M. J.; Tso, T.; Molina, L. T.; Wang, F. C. *Science (Washington, D.C.)* **1987**, *238*, 1253.
(14) Tolbert, M. A.; Rossi, M. J.; Malhotra, R.; Golden, D. M. *Science (Washington, D.C.)* **1987**, *238*, 1258.
(15) Gardner, J. A.; Watson, L. R.; Adewuyi, Y. G.; Davidovits, P.; Zahniser, M. S.; Worsnop, D. R.; Kolb, C. E. *J. Geophys. Res.* **1987**, *92*, 10887.
(16) Berglund, R. N.; Liu, B. Y. H. *Environ. Sci. Technol.* **1973**, *7*, 147. Ashgriz, N.; Yao, S. C. *Rev. Sci. Instrum.* **1987**, *58*, 1291; Schneider, J. M.; Hendricks, C. D. *Rev. Sci. Instrum.* **1964**, *35*, 1349. Strom, L. *Rev. Sci. Instrum.* **1969**, *40*, 778.
(17) Rayleigh, J. W. S. *Proc. R. Soc.* **1879**, *29*, 71.

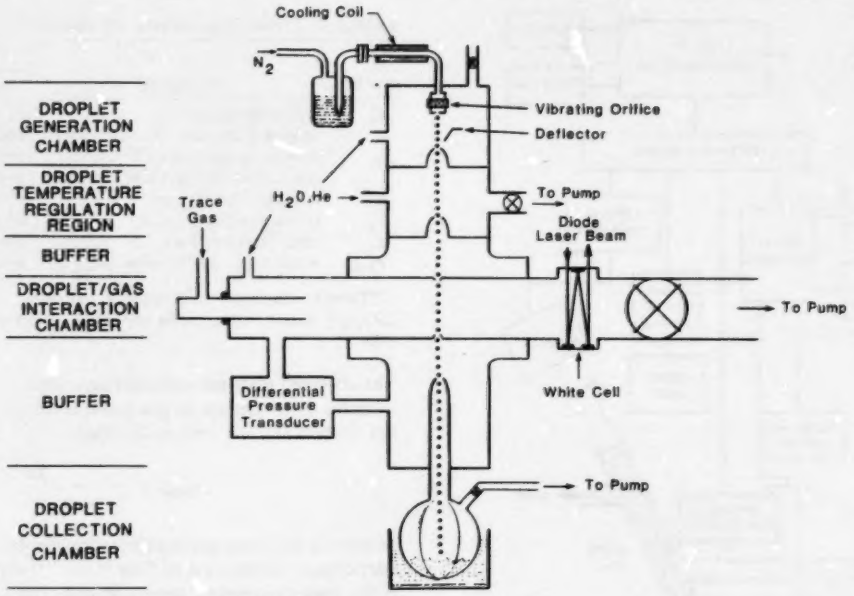

Figure 2. Schematic of transverse droplet–gas flow apparatus.

In both apparatuses the droplet train passes through a cylindrically focused HeNe laser (shown in Figure 1) to monitor droplet diameter and velocity. Figure 3 shows oscilloscope traces of attenuated laser intensity for two different droplet frequencies and diameters.

Total gas flow is measured by the pressure rise in a calibrated volume when the pump line is temporarily closed. Rare gas flows are measured with calibrated rotameters before introduction into the flow tube.

A key aspect of the experiment is the maintenance of equilibrium between ambient water vapor and the droplet train temperature. This equilibrium is monitored by measuring changes in pressure in all vacuum chambers as the droplet surface area is changed. In the transverse apparatus, there is an additional differential pressure transducer that continuously monitors the pressure difference between the flow tube and buffer chamber in Figure 2. Overall balance in the flow tube is checked further by monitoring the concentration of a reference gas, in this case methane. Because methane is effectively insoluble in water, any change in methane concentration with droplet switching determines the "zero" of the system and is subtracted from observed changes in trace gas concentration.[15]

In the coaxial apparatus, droplet temperature is measured directly with a thermocouple placed in the deflector in the droplet generation chamber. This is possible for droplet temperatures above 273 K. For supercooled droplets in the transverse apparatus, direct measurement is not feasible since the droplets freeze on contact with a surface. In this case the droplet temperature is inferred from ambient water vapor pressure when system pressure balance upon droplet switching indicates that the droplets are in equilibrium with the ambient atmosphere. Water vapor content in the flow tube is calculated by subtracting all inert gas flows from the total flow.

Sulfur dioxide (Matheson, anhydrous SO_2, 99.98%) is premixed to 5% in helium in a 1-L tank at 5 psig. Hydrogen peroxide flow was controlled by passing helium through a bubbler containing 50% H_2O_2 solution (Fisher, stabilized) in an ice bath. Filtered water (Millipore, Milli-Q) was used to generate droplets.

Tunable Diode Laser Absorption. Trace gas concentrations are measured by infrared differential absorption using a tunable diode laser (Laser Analytics) with a multiple-pass "White" cell connected to the downstream end of the reaction chamber, as shown in Figure 1. The tunable diode laser system provides a universal detection method for heteronuclear gaseous molecules. The laser frequency is tuned to a single rovibrational line of the trace gas. Several lines of SO_2 around 1352 cm^{-1} have line strengths of the order of 6×10^{-20} cm^2 $molecule^{-1}$ cm^{-1},[18] resulting

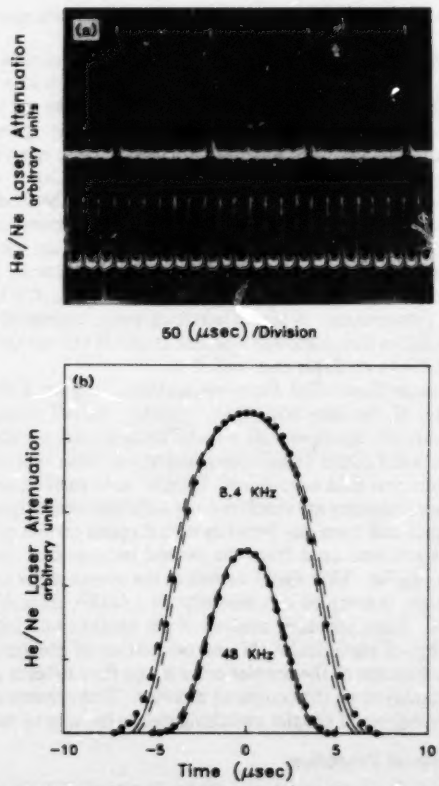

Figure 3. (a) Oscilloscope traces of HeNe laser attenuation for droplet trains at two different frequencies. The vertical axis has been shifted for clarity for the two traces. (b) Expanded traces (digitized points) for single droplets. For liquid flow rate 0.08 cm^3 s^{-1} through a 61-μm orifice, labeled frequencies correspond to 146- and 261-μm droplets. Curves described in text; dashed lines calculated by changing droplet velocity ±5%.

(18) Rothman, L. S.; Goldman, A.; Gillis, J. R.; Gamache, R. R.; Pickett, H. M.; Poynter, R. L.; Husson, N.; Chedrin, A. *Appl. Opt.* **1983**, *22*, 1616.

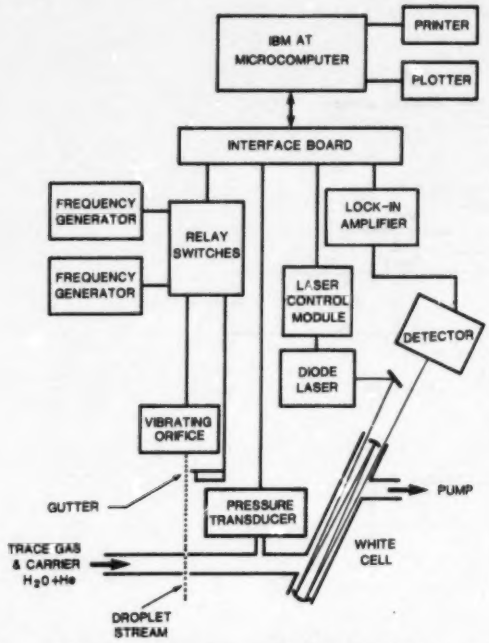

Figure 4. Schematic of computer control/data acquisition system.

in a fractional absorption of $\Delta I/I_0 = 0.01$ for a concentration of $[SO_2] = 1 \times 10^{12}$ molecules cm^{-3} in the 728-cm path length cell. For H_2O_2, line strengths around 1252 cm^{-1} are of the same order of magnitude. Typical trace gas concentrations ranging from 1.5×10^{12} to 1.5×10^{13} molecules cm^{-3} are used in these experiments. The best signal-to-noise ratio is obtained by using a second harmonic signal, which is produced by modulating the diode laser frequency around the line center frequency and processing the signal with a lock-in amplifier at twice the modulation frequency of 1 kHz. The output of the lock-in amplifier is linear with trace gas concentration at the low optical depths ($\Delta I/I_0 < 0.1$) used in these experiments. A piezoelectric ceramic, cemented to one of the White cell mirrors, was vibrated at 160 Hz to reduce etalon fringing in the multiple pass cell.[19]

Computer-Controlled Data Acquisition. Figure 4 shows a schematic of the data acquisition system. An AT compatible microcomputer, equipped with a multifunction analog and digital interface board (Data Translation), actively controls experimental parameters and data acquisition. Droplet train surface area and diode laser frequency are synchronously switched for determination of reference and trace gas densities with droplets on and off. Gas densities are measured from the second harmonic output of a lock-in amplifier. That signal, as well as the output of the pressure transducers, is sampled continuously via a DMA channel of the computer. Thus, real-time analysis of gas uptake rates, including calculation of statistical S/N and estimation of pressure/temperature balance of the droplet train in the flow tube, is continuously displayed on the computer monitor. This permits routine signal averaging of droplet switching cycles for tens of minutes.

Experimental Procedure

The experiment measures the change in trace gas concentration as a function of the water droplet surface area to which the gas flow is exposed. The experimental approach permits a relatively simple interpretation of the measured trace gas uptake rate to obtain a mass accommodation coefficient. The mass accommodation coefficient (γ) is defined as

$$\gamma = \frac{\text{number of molecules absorbed by droplets}}{\text{number of molecular collisions with droplets}}$$

(19) Anderson, S.; Zahniser, M. S. Aerodyne Research, Inc., unpublished results, 1987.

TABLE I: Typical Experimental Parameters

symbol	parameter	apparatus: coaxial	apparatus: transverse
d_o	orifice diam, μm	61 (22)	61
d	droplet diam, μm	140 (80)	140/270[a]
v_d	droplet velocity, cm s^{-1}	1600–4400	2700
l	gas–droplet interact dist, cm	4–20.5	2.7
n	trace gas density, cm^{-3}	10^{13} (10^{15})[b]	10^{13}
F_g	vol rate of flow, cm^3 s^{-1}	40–200	250–800
P	total pressure, Torr	10–50	2.3–10
P_{H_2O}	water vapor partial pressure, Torr	8–18	2–8

[a] Droplet diameters in frequency switching experiment. [b] Higher $[SO_2(g)]$ density experiments utilized a 10-cm single-pass absorption cell.

The observed mass accommodation coefficient may be expressed in terms of the change in gas-phase trace gas concentration n as the droplet surface area is changed:

$$\gamma_{obsd} = \frac{F_g}{\frac{1}{4}\bar{c}NA_d}\frac{\Delta n}{n} \quad (1)$$

where n is the trace gas concentration (molecules cm^{-3}), F_g is the carrier gas volume rate of flow (cm^3 s^{-1}) through the system, $\bar{c}$ is the trace gas average thermal velocity (cm s^{-1}), N is the number of droplets to which the trace gas is exposed, and A_d is the surface area of each droplet (cm^2). The numerator in eq 1 gives the number of molecules removed from the gas phase per unit time, while the denominator gives the total number of molecular collisions with droplet surfaces. As mentioned earlier, due to gas diffusion and surface saturation considerations γ_{obsd} in eq 1 is in general only a lower limit to the "true" γ due to gas diffusion and surface saturation considerations. In the analysis below we deconvolute these effects from γ_{obsd} to obtain γ.

Table I lists typical values of the experimental parameters that were used to measure γ_{obsd} in each of the apparatuses. Below we discuss the experimental considerations that determine the validity of eq 1 for calculating γ_{obsd}: the gas flow down the flow tube, the droplet surface area to which the gas is exposed, the measurement of changes in trace gas concentration, and the droplet temperature, which is controlled by equilibration with the ambient water vapor.

Gas Flow Considerations. Equation 1 is based on gas kinetic theory which predicts that the flux of molecules through a plane is given by $n\bar{c}/4$. Interpretation of our data depends on the knowledge of n in the vicinity of the droplets as well as the applicability of the expression.

The coaxial apparatus is similar in principal to a conventional flow tube for homogeneous kinetic studies operating under conditions of plug flow where diffusion across the tube is sufficiently rapid to minimize radial concentration gradients, and the flow velocity ($\bar{v}$) is fast compared to diffusive transport in the axial direction. Thus there is a concentration gradient along the length of the flow tube, x, such that

$$dn/dx = -k^1 n/\bar{v}$$

where k^1 is the first-order rate constant for trace gas loss to the droplet surface:

$$k^1 = \frac{1}{4}\bar{c}\gamma NA_d/V$$

This is similar to the expression given by Kaufman[20] for wall loss in a cylindrical flow reactor except that the surface-to-volume ratio in this case is NA_d/V, where V is the total flow tube volume. Integrating the loss rate over the length of the flow tube, l, gives

$$\ln (n/n') = k^1 l/\bar{v}$$

where n and n' are the gas concentrations at the inlet and outlet of the flow tube, respectively. Upon rearrangement this gives

(20) Kaufman, F. *Progress in Reaction Kinetics*; Pergamon: New York, 1961; Vol. 1, p 3.

$$\gamma = \frac{F_g}{\frac{1}{4}\bar{c}NA_d} \ln (n/n') \quad (2)$$

where $F_g = V\bar{v}/l$ is the volume rate of flow of the carrier gas.

The above expression is accurate in the limit that axial transport by diffusion is small compared to the flow velocity. The correction to the observed first-order rate constant, k_{obsd}, is[20]

$$k^I = k_{obsd}(1 + k_{obsd}D/\bar{v}^2)$$

For our typical experimental conditions with $\bar{v} \geq 30$ cm s^{-1}, $D = 5$ cm^2 s^{-1}, $NA_d = 0.1$ cm^2, and $V = 36$ cm^3, a value of $\gamma = 0.1$ corresponds to $k_{obsd} = 2$ s^{-1}, making the above correction factor less than 1%. This is small enough to be neglected, and γ_{obsd} is calculated directly from eq 2 for the coaxial apparatus.

For the transverse apparatus the droplet stream is orthogonal to the flow axis so that the molecules removed by the droplets are continually replenished by convective transport. If both the flow velocity ($\bar{v} \geq 30$ cm s^{-1}) and the pressure-dependent diffusion coefficient ($D \geq 20$ cm^2 s^{-1}) are large enough, then the combination of diffusion and convection is sufficient to maintain the trace gas concentration in the vicinity of the droplets. γ_{obsd} may then be calculated from eq 1. This is experimentally verified by the independence of γ_{obsd} with flow velocity.

Equations 1 and 2 assume the surface collision rate is given by $n\bar{c}/4$ as predicted by the Maxwellian velocity distribution of gas kinetic theory. If there is significant surface uptake, the expression for γ must be corrected by[21]

$$\gamma = \frac{\gamma_0}{1 + \gamma_0/2} \quad (3)$$

where γ_0 is the zero-pressure limit of γ_{obsd} (see below). This correction takes into account the fact that loss at a surface distorts the Maxwellian velocity distribution. Molecules with velocity vectors pointing toward the surface are selectively removed, giving the velocity distribution a net velocity toward the surface, thus increasing the surface collision rate. In the limit of a mass accommodation coefficient of unity, this approximation predicts $\gamma_0 = 2$ calculated from eq 1.

Droplet Surface Area. The aqueous surface area to which the trace gas is exposed is calculated from the number and size of droplets in the flow tube. The volume of each droplet is given by the liquid flow rate through the orifice (F_l) divided by the droplet frequency (f_d). Assuming that the droplets are spherical, the droplet diameter is

$$d = (6F_l/\pi f_d)^{1/3} \quad (4)$$

The number of droplets to which the gas flow is exposed is

$$N = lf_d/v_d$$

where l is the droplet–gas interaction distance and v_d the droplet velocity. The latter is calculated from F_l and the orifice diameter (d_o):

$$v_d = 4F_l/\pi d_o^2 \quad (5)$$

The exposed droplet surface area is given by

$$A = NA_d = l\pi d_o^2(9\pi f_d/16F_l)^{1/3} \quad (6)$$

where A_d is the area of an individual droplet calculated from a sphere of diameter d. When the droplet train is mechanically switched on and off with the deflector, then eq 6 directly gives the exposed surface area used in eq 1 or 2. When the surface area is varied by switching the droplet frequency, as it was for the majority of data taken in the transverse apparatus, then A is given by the difference in the A values calculated from eq 6. Since the total exposed area is proportional to $f_d^{1/3}$, a factor of 8 in droplet frequency gives a factor of 2 change in the exposed surface area.

The above calculation assumes there is no significant slowing down of the droplet velocity in the low-pressure atmosphere. The validity of this assumption is confirmed by HeNe laser attenuation traces for droplet trains at two different frequencies shown in Figure 3. The symmetry of the digitized points in Figure 3b confirms that the droplets are spherical. The curves were calculated by passing a circular silhouette of a droplet through a 40-μm ($1/e^2$) Gaussian profile of the focused HeNe laser beam. The relative height of the traces for the different frequency drops is a direct measure of their relative diameter. The widths on the time axis are an absolute measure of the ratio of droplet diameters and velocities. The fit of the calculated curves to the points indicates that d and v_d are known to better than 5%. The self-consistent fit to both droplet sizes indicates there is no significant slowing of the droplets due to atmospheric drag.

It should be noted, as is apparent from Figure 3, that for a given orifice diameter the size and spacing of the droplets are not independent. The smaller the frequency, the larger *and* more widely spaced are the droplets. Size and spacing can be varied independently only by using orifices of different size. Two orifice sizes, 22 and 61 μm in diameter, were used in the experiments reported here. Table I shows the typical droplet diameter generated with each orifice. The full range was 60–180 and 110–270 μm for the 22- and 61-μm orifices, respectively. Thus, in these experiments spacing was varied by a factor of 3 for droplets 110–180 μm in diameter.

Droplet Temperature Control. Any liquid will actively equilibrate its temperature with its ambient vapor by either condensation or evaporation. In the case of water, this temperature equilibration is particularly efficient because the heat of vaporization of water (45 kJ mol^{-1}) is so much larger than its heat capacity (0.08 kJ mol^{-1} K^{-1}). For example, a 10 K cooling of water corresponds to evaporation of about 2% of its volume. The heat of vaporization is also much larger than the thermal energy of the surrounding gas molecules. For example, a temperature difference of 30 K between the ambient atmosphere and the droplet train corresponds to an energy difference of $k\Delta T = 0.2$ kJ mol^{-1}. This indicates that evaporative cooling will maintain the droplet surface temperature even though the flow tube walls are at room temperature.

In our experiment, liquid water is forced through the orifice at a temperature T_o and enters the flow tube a few milliseconds later. For experiments where droplet temperatures are above 273 K (i.e., ambient water vapor pressure >4.6 Torr), the water can be precooled to the final desired droplet temperature (T). For lower temperatures, droplets are supercooled evaporatively. The final droplet T was as much as 17 K colder than T_o of the water leaving the orifice. To quantitatively evaluate the degree of temperature equilibration between droplets and ambient atmosphere, one must consider the rate of evaporation or condensation compared to the millisecond experimental time scale. Moreover, when the droplet train is colder than the room-temperature apparatus, the heat flux between the gas and the droplets and the corresponding temperature gradient in the gas must also be considered.

These temperature equilibration rates are discussed in detail in the Appendix. The overall result is that the droplet surface equilibrates very quickly with ambient water vapor. However, for droplets ≥100 μm in diameter, the interior volume of the droplet does not equilibrate on the millisecond experimental time scale. This results in a continuous evaporative flux from the droplets that implies that the droplet train cannot be in simultaneous pressure and temperature equilibrium with the flow tube. To avoid spurious flows in or out of the flow tube holes, it is desirable to maintain net pressure balance in the flow tube as the droplet train is switched. This is achieved by cooling the droplet surface slightly below equilibrium temperature corresponding to the water vapor partial pressure in the flow tube. The droplet train then condenses just enough water vapor upon entering the flow tube to compensate for evaporation due to the thermal flux from the droplet interior.

The analysis in the Appendix indicates that for a given set of conditions a measured trace gas uptake rate represents an average over a range of up to 2 K around the desired equilibrium temperature. For the worst case of droplets supercooled to 260 K, there will be an average difference in surface temperature of about

(21) Motz, H.; Wise, H. *J. Chem. Phys.* **1960**, *32*, 1893.

0.4 K between different diameter droplets in frequency switching experiments. The other major source of error is the measurement of the water vapor partial pressure. An uncertainty of up to 15% corresponds to an uncertainty of up to 2 K in water temperature. These uncertainties are largest at the lowest temperatures (T = 260 K) and decrease to ≤0.5 K as T approaches room temperature.

Droplet/Flow Tube Balance. This picture of temperature and pressure equilibration is qualitatively confirmed by the observation of pressure balance in the measurements reported here. In all experiments, the total pressure in the flow tube is continuously monitored as the droplet train is switched. A net change in pressure can be converted to a flux of water molecules per drop by using the gas flow rate and pressure and the number and frequency of droplets in the flow tube. In the coaxial apparatus, for typical flow and pressure conditions of 5 scc s^{-1} and 20 Torr, an observed 1% pressure change corresponds to a flux of 3×10^{12} molecules from each drop. In the transverse apparatus, continuous monitoring of the differential pressure between the flow tube and the adjacent buffer chamber permitted maintenance of pressure stability approaching 0.1%. For frequency switching experiments at 5 Torr, observed pressure changes of ≤0.2% corresponded to fluxes of $\leq 5 \times 10^{11}$ molecules to or from each drop. These fluxes are consistent with those predicted in the Appendix for temperature balance better than ≤1 K.

The only systematic deviation from these observations occurred in experiments with 58% added Ar. Pressure changes observed upon droplet frequency switching corresponded to temperature differences between the 140- and 270-μm droplets of up to 3 K. This was due to the fact that the water vapor evaporation rates in Ar atmospheres are somewhat gas-diffusion limited.

Overall balance of both flows and possible losses in or out the entrance or exit holes in the flow tube is monitored by measuring changes in methane reference gas concentration. The fractional change in methane concentration observed with droplet switching provides a "zero" level which is subtracted from the observed fractional change in the trace gas. Extensive testing of this correction on the coaxial apparatus indicates that the corrected trace gas fractional change is indeed the actual uptake into the droplet train.[15]

In the transverse apparatus, we have established that even when relative and absolute system pressures are perfectly balanced, there is a net change of the order of 0.5% in the methane under typical operating conditions (see Table I). The cause of this was observed in a flow visualization experiment based on the reaction

$$O + NO \xrightarrow{M} NO_2^* \rightarrow NO_2 + h\nu$$

Oxygen atoms were passed down the flow tube and NO introduced into the buffer chamber. Gas mixing between the flow tube and the buffer chamber could be observed from the green chemiluminescence from NO_2^*. Under conditions of pressure balance, green "puffs" several millimeters in diameter could be seen diffusing out both the entrance and exit holes of the flow tube (see Figure 2). When the droplet train was switched on, the top "puff" disappeared and the bottom one increased in size. The net CH_4 depletion observed under these conditions indicates that the train has the net effect of sweeping some gas out the bottom hole. The observation of this transport effect underscores the importance of checking gas balance with the methane reference gas.

Sensitivity. Table I lists typical operating conditions for the two apparatuses. The detection limit of the diode laser after signal averaging corresponds to a fractional absorption of about 10^{-5}. For an initial trace gas absorption level of 1%, this corresponds to fractional uptake by the droplet train of about 0.1%. This gives 0.5% as the minimum fractional depletion detectable with signal-to-noise >5. For the flow conditions listed in Table I, this corresponds to mass accommodation coefficients of about 10^{-2} and 10^{-3} in the transverse and coaxial apparatuses, respectively. Using slower flows and larger (stable) trace gas concentrations lowers these limits another order of magnitude. At these minimum depletion levels, the absolute accuracy of the reference gas correction for hole effects would become the most significant systematic uncertainty.

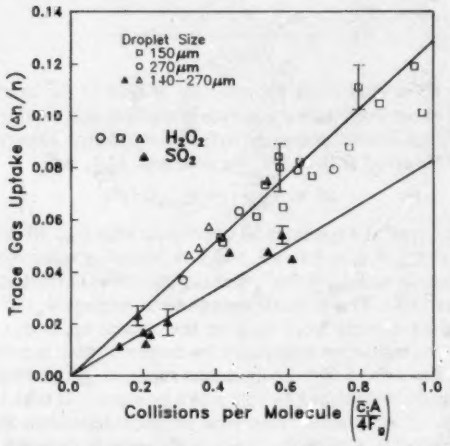

Figure 5. Data from the transverse apparatus for SO_2 and H_2O_2 plotted according to eq 1. Water vapor partial pressure ~ 5 Torr (droplet temperature = 274 K). Slopes of the best-fit lines yield $\gamma_{obsd}(H_2O_2)$ = 0.129 ± 0.009 and $\gamma_{obsd}(SO_2)$ = 0.083 ± 0.009.

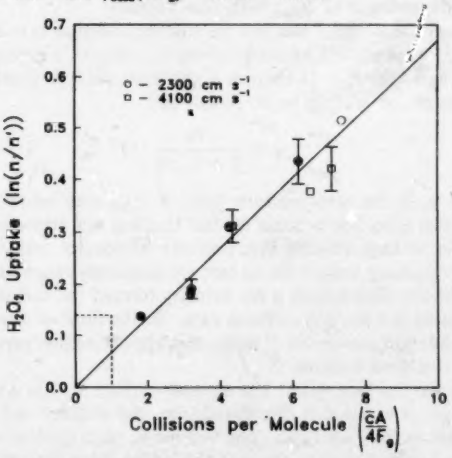

Figure 6. Data from the coaxial apparatus for H_2O_2 uptake plotted according to eq 2. Water vapor partial pressure ~ 16 Torr (droplet temperature = 292 K). The best-fit line yields γ_{obsd} = 0.067 ± 0.006. The dashed rectangle in the lower left corner shows the range of parameters in Figure 5 for the transverse apparatus.

Results

These experiments were designed to determine absolute mass accommodation coefficients of trace gases on aqueous surfaces while investigating the effects of gas diffusion, droplet temperature, and surface saturation. We report the results of more than 200 runs that measured SO_2 and H_2O_2 uptake as a function of several experimental parameters. Variations of pressure, atmospheric composition, and droplet size were used to determine gas-phase diffusion rates. Variations of trace gas density, gas/droplet contact time, and, in the case of SO_2, droplet pH were used to determine surface saturation limitations. Variation of droplet temperature by changing the water vapor content of the experimental atmosphere was used to determine the effect of surface temperature on the uptake rate.

Figures 5 and 6 plot the basic relations between trace gas uptake and molecular collisions with the water droplet surface in the transverse and coaxial apparatuses. The ordinate of Figure 5 is the measured fractional uptake (eq 1) for SO_2 and H_2O_2 data from the transverse apparatus in an atmosphere of about 5 Torr of water vapor. The abscissa is the dimensionless quantity $\bar{c}A/4F_g$, which gives the average number of collisions with the total droplet surface for each molecule of trace gas during its transit time through the flow tube. Figure 6 is a plot (eq 2) for H_2O_2 data from the coaxial apparatus at about 20 Torr. The slope of each plot gives the uptake rate expressed as an observed mass accommodation

coefficient (γ_{obsd}). The corresponding plot of SO_2 uptake measured in the coaxial apparatus from our previous work[15] has a slope of $\gamma_{obsd} = 0.054 \pm 0.006$, similar to that of H_2O_2 in Figure 6. The quoted errors are all 3σ for the standard uncertainties in the slopes. Each point in Figures 5 and 6 is the average of 6–20 droplet switching cycles for both the methane reference gas and the trace gas, representing signal averaging times of 3–20 min.

The dashed rectangle in the lower left-hand corner of Figure 6 displays the range of parameters of the plot in Figure 5, indicating how the two apparatuses complement one another in the range of contact between trace gas and aqueous surface area. The linearity of data plotted according to eq 1 and 2 for a variation factor of 50 in the abscissa validates the kinetic measurement of the trace gas uptake rate. In the case of SO_2, analysis of the S(IV) content of collected water droplets in the coaxial apparatus confirmed that the observed SO_2 gas-phase depletion was indeed due to uptake into the droplet stream.[15]

The slopes for both H_2O_2 and SO_2 in Figure 5 ($\gamma_{obsd} = 0.129$ and 0.083, respectively) measured in the transverse apparatus are significantly larger than the corresponding values in Figure 6 for H_2O_2 and the previously reported SO_2 result[15] ($\gamma_{obsd} = 0.067$ and 0.054, respectively) measured in the coaxial apparatus. These experiments were performed at different system pressures, resulting in differences in the rate of gas-phase diffusion and in droplet temperature. Because gas-phase diffusion rates increase with lower pressure, one expects γ_{obsd} to increase with decreasing total system pressure. At the same time, the ambient water vapor pressures of about 5 and 16 Torr in Figures 5 and 6 correspond to droplet temperatures of about 274 and 292 K, respectively. The larger increase in γ_{obsd} for H_2O_2 (0.129/0.067 = 1.93) compared to that of SO_2 (0.083/0.054 = 1.54) indicates that H_2O_2 has a stronger negative temperature dependence than SO_2. Below we discuss in depth the complete pressure dependence of γ_{obsd} for SO_2 and H_2O_2 over the range of 2–50 Torr. The goal of the analysis is to deconvolute the gas-diffusion rate and the heterogeneous uptake rate to directly obtain the temperature dependence of the mass accommodation coefficient.

Surface Saturation. The degree of saturation of a liquid surface exposed to a trace gas is a function of both the solubility of the gas and the length of time the gas and liquid are exposed to one another. In our experiment, the contact time between an individual droplet and the flow tube atmosphere is determined by the droplet–gas interaction distance divided by the droplet velocity. For the data of Figure 6 for H_2O_2, these parameters were varied to give a range of 2–13 ms for this droplet–gas contact time. The linearity of the observed H_2O_2 uptake plot in Figure 6 is consistent with there being no significant reevaporation of absorbed H_2O_2 during the time scale of that data. This indicates that the Henry's law solubility of H_2O_2 ($\approx 10^5$ M atm^{-1})[22] is large enough to minimize surface saturation, maintaining a gas/liquid concentration gradient that permits direct kinetic measurement of the mass accommodation rate.

In the case of SO_2, surface saturation is negligible only when the initial pH of the droplet stream is adjusted to be basic (e.g., pH = 11.2 in Figure 5).[15] This is shown in Figure 7, which plots γ_{obsd} versus droplet/gas contact time. The upper points, at droplet initial pH = 11.2 and $[SO_2]_g = 10^{13}$ cm^{-3}, show little variation of uptake rate with contact time, consistent with the $\gamma_{obsd} = 0.054$ previously reported.[15] However, the lower points, at initial pH = 4 and $[SO_2]_g = 10^{15}$ cm^{-3}, show a marked decrease in uptake rate with longer contact time, down to $\gamma_{obsd} = 0.002$ after 13 ms.

These observations are due to the fact that sufficient aqueous solubility of gaseous SO_2 occurs only upon its (pH dependent) dissociation into bisulfite and sulfite anions described by the equilibria

$$SO_2(g) \rightleftarrows SO_2(aq) \qquad H_{SO_2}$$

$$SO_2(aq) + H_2O \rightleftarrows H^+ + HSO_3^- \qquad K_{a1}$$

$$HSO_3^- \rightleftarrows H^+ + SO_3^{2-} \qquad K_{a2}$$

(22) Martin, L. R.; Damschen, D. E. *Atmos. Environ.* **1981**, *15*, 1615.

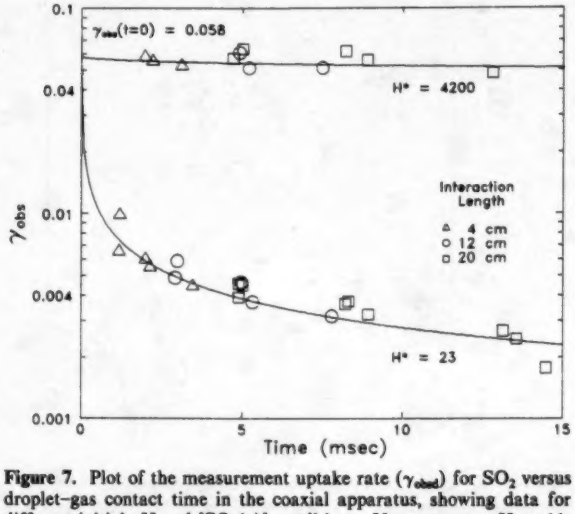

Figure 7. Plot of the measurement uptake rate (γ_{obsd}) for SO_2 versus droplet–gas contact time in the coaxial apparatus, showing data for different initial pH and $[SO_2(g)]$ conditions. Upper curve: $pH_0 = 11$; $[SO_2(g)] \sim 10^{13}$ molecules cm^{-3}. Lower curve: $pH_0 = 4$; $[SO_2(g)] \sim 10^{15}$ molecules cm^{-3}. Droplet–gas contact time is varied by changing the droplet–gas interaction distance and droplet velocity. Curves are calculated from eq 11.

As pointed out by Schwartz,[4] the solubility of SO_2 can be expressed as an effective Henry's law constant given by

$$H^*_{S(IV)} = H_{SO_2}\left(1 + \frac{K_{a1}}{[H^+]} + \frac{K_{a1}K_{a2}}{[H^+]^2}\right)$$

where $H = 1.3$ M atm^{-1} is the physical Henry's law constant for SO_2 at 20 °C.[23] The effective Henry's law is dependent on the SO_2 gas-phase density, since SO_2 dissolution acidifies the liquid, thus changing the pH and shifting the equilibria. Assuming that the gas-phase SO_2 is always in equilibrium with SO_2(aq) at the surface of the liquid droplet, one can calculate the pH at the droplet surface by solving the equilibria to give

$$[H^+] = H' \pm (H'^2 + K_w + K_{a1}[SO_2])^{1/2}$$

where

$$H' = ([H^+]_0 - K_w/[H^+]_0)/2$$

where $[H^+]_0$ is the initial H^+ concentration and K_w is the equilibrium constant for water (10^{-14} M^2). This derivation assumes the second dissociation to SO_3^{2-} is negligible. This is true for surface pH < 7, with $K_{a1} = 1.39 \times 10^{-2}$ M and $K_{a2} = 6.5 \times 10^{-8}$ M.[24] Thus, in Figure 7 the listed $[SO_2(g)]$ and pH conditions for the upper and lower sets of points correspond to effective Henry's law solubilities of 4200 and 23 M atm^{-1}, respectively.

The decrease in observed uptake rate of SO_2 with time in the lower curve of Figure 7 is due to reevaporation of dissolved SO_2 as the droplet surface becomes saturated in S(IV). The exact time dependence of γ_{obsd} is a convolution of the effective solubility and the rate of liquid-phase diffusion into the interior of the droplet. This can be modeled by calculating the time-dependent S(IV) concentration at the liquid surface. We begin by expressing the uptake rate in terms of the liquid-phase concentration, relating liquid- and gas-phase concentrations by Henry's law:

$$H^* = \frac{n_1^0}{RTn_g} \tag{7}$$

The time-dependent flux to the surface can be expressed as

$$J = \frac{\bar{c}\gamma_{obsd}(t)}{4RTH^*}[n_1^0 - n_1(t)] \tag{8}$$

(23) Wilhelm, E.; Battino, R.; Wilcox, R. J. *Chem. Rev.* **1977**, *77*, 219.
(24) Goldberg, R. N.; Parker, V. B. *J. Res. Natl. Bur. Stand.* **1985**, *90*, 341.

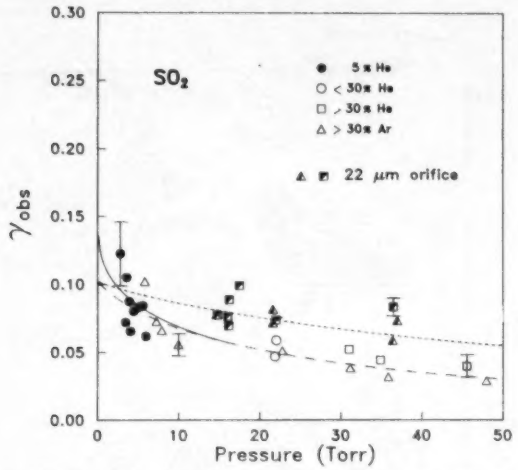

Figure 8. SO_2 uptake rates (γ_{obsd}) versus total system pressure for various atmospheric compositions. Curves calculated by convoluting temperature dependence of eq 16 with diffusion-limited rate of eq 15. Dashed curves assumes $\Delta E = 0$ for 22- and 61-μm orifices, upper and lower curves, respectively. Solid curve uses best-fit $\Delta E = -2$ kJ mol^{-1} from Figure 14.

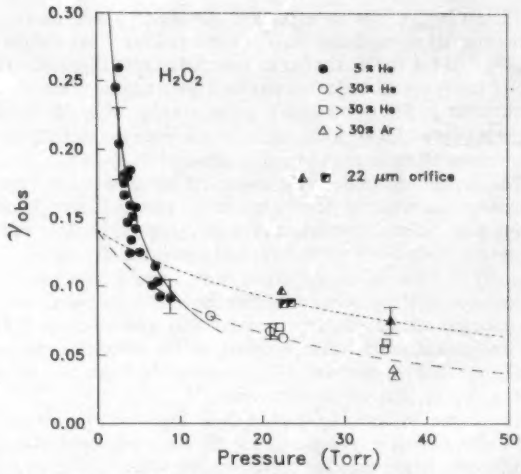

Figure 9. H_2O_2 uptake rates (γ_{obsd}) versus total system pressure for various atmospheric compositions. Dashed curves assumes $\Delta E = 0$ for 22- and 61-μm orifices, upper and lower curves, respectively. Solid curve uses best-fit $\Delta E = -26$ kJ mol^{-1} from Figure 13.

where $n_l(0) = 0$. This is equivalent to eq 1 which implicitly assumed that $n_l(t) \ll n_l^0$. We can approximate $n_l(t)$ as the average concentration in some penetration depth dx:

$$n_l(t) = \frac{Jt}{dx} \tag{9}$$

where dx can be approximated by the liquid diffusion depth:

$$dx = (D_l t)^{1/2} \tag{10}$$

where D_l is the diffusion coefficient of the trace species in the liquid. ($D_l = 1.8 \times 10^{-5}$ cm^2 s^{-1} for SO_2 in water at 298 K).[25] This expression for dx assumes that dx is much smaller than the droplet radius.

Combining eq 7–10, we obtain

$$\gamma_{obsd}(t) = \frac{1}{\frac{1}{\gamma_{obsd}(t=0)} + \frac{\bar{c}}{4RTH^*}\left(\frac{t}{D_l}\right)^{1/2}} \tag{11}$$

An equation similar to this has been derived more rigorously by Schwartz and Freiberg.[5] Also, Danckwerts reported the exact analytical solution for the time-dependent uptake into a spherical drop.[26] For our conditions, there is no significant difference between eq 11 and that analytical solution.

The curves in Figure 7 were calculated by fitting $\gamma_{obsd}(t=0)$ to the intercept of the upper points with the large $H^* = 4200$ using a linear least-squares fit to $1/\gamma_{obsd}(t)$ versus $t^{1/2}$. The agreement of the lower curve ($H^* = 23$) to the points is an absolute measure of the product of $H^*(D_l)^{1/2}$ and the millisecond experimental time scale. The fit of both curves to the data using the same $\gamma_{obsd}(t=0)$ indicates that γ is independent of droplet pH.

The fit to the upper curve gives a value of $\gamma_{obsd} = 0.058 \pm 0.006$ for SO_2 at 291 K in an atmosphere of 18 Torr of water vapor + 5 Torr of He. This represents a slight correction to our reported value of 0.054, which assumed there was no saturation limitation. All the observed uptake rates for SO_2 we report below have been corrected for this saturation limitation. All the data were taken with $pH_0 \geq 11$, $[SO_2]_g \leq 10^{13}$ cm^{-3}, and $t \leq 12$ ms, so that the correction was <10%. Thus, γ_{obsd} with no argument always refers to the extrapolated $\gamma_{obsd}(t=0)$.

Pressure Dependence. Figures 8 and 9 display the pressure dependence of the observed SO_2 and H_2O_2 uptake rates (γ_{obsd}). The pressure plotted is the total system pressure; different symbols refer to different composition, ranging from 95% water vapor up to 80% added He or Ar. The majority of the data were taken with droplet trains generated with a 61-μm diameter orifice; the half-shaded points used a 22-μm orifice. Each point is an average of 1–6 runs as described above. The slopes of the lines in Figures 5 and 6 (and the upper curve of Figure 7) each represent one point in Figures 8 and 9. Representative error bars are 1σ standard deviations of the mean.

The pressure dependence is a convolution of the dependence on temperature and gas diffusion. Droplet temperature is controlled by equilibration with ambient water vapor pressure. A range of H_2O partial pressure of 2–18 Torr in the data of Figures 8 and 9 corresponds to 260–294 K droplet temperature. At the same time, the rate of gas-phase diffusion increases with lower pressure. One expects the observed accommodation rate (γ_{obsd}) to increase with decreasing pressure, approaching γ_0 (the zero-pressure limit) when the heterogeneous uptake rate is independent of the rate of gas-phase mass transport.

Variation of the gas diffusion rate can be seen directly in the higher pressure data of Figures 8 and 9. In these experiments the water vapor partial pressure was kept at about 16 Torr, corresponding to a constant droplet temperature of 292 K. Thus, the decrease in γ_{obsd} as total pressure was increased above 16 Torr is due entirely to slower diffusion. γ_{obsd} values are also larger for the data taken with the 22-μm orifice, since gas mass-transport rates increase with smaller droplets. Quantitative analysis of these gas-diffusion effects must take into account atmospheric composition, since diffusion rates in water vapor, He and Ar differ.

The distinctive feature of Figures 8 and 9 is the qualitative difference between the pressure dependence of the SO_2 and H_2O_2 uptake rates at low pressures. The relatively small increase in γ_{obsd} for SO_2 at low pressure appears to be a continuation of the trend at high pressure, consistent with an increasing gas-phase diffusion rate at lower pressure. The much steeper increase in H_2O_2 uptake rate as the total pressure (and water vapor) decreases below 15 Torr is consistent with a heterogeneous H_2O_2 uptake rate that increases with decreasing droplet temperature.

This temperature dependence of γ_{obsd} for H_2O_2 is clearer in Figure 10, which expands the pressure scale of Figure 9 for the H_2O_2 data. This plot includes other low-pressure data taken with Ar (58%) or He (68%) added to separate the effects of gas diffusion and droplet temperature on the uptake rate. For these latter data, a given total pressure contains a lower water vapor pressure than the corresponding (nearly) pure water vapor points (solid circles). Thus, the temperature scale for the added rare-gas points (open triangles and squares) is effectively shifted to the right compared to the pure water points. The larger values of γ_{obsd} for the added rare-gas points correspond to these lower temperatures,

(25) Leaist, D. G. *J. Chem. Eng. Data* **1984**, *29*, 281.
(26) Danckwerts, P. V. *Trans. Faraday Soc.* **1951**, *47*, 1014.

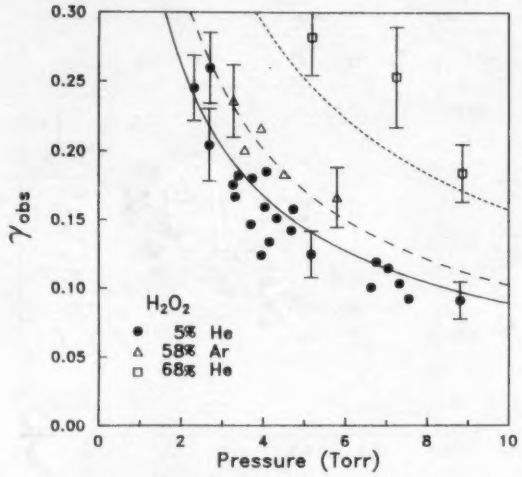

Figure 10. Expanded plot of Figure 9 for low-pressure data for H_2O_2 from the transverse apparatus. Additional data points with added He and Ar show temperature dependence of γ for H_2O_2 as described in the text.

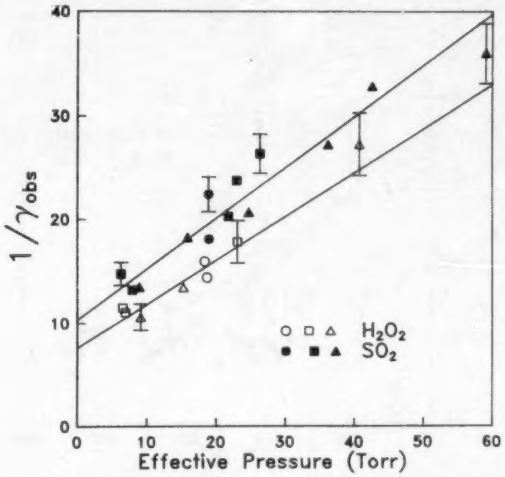

Figure 11. Variation of gas-diffusion-limited uptake (eq 14) for H_2O_2 and SO_2 at constant droplet temperature $T = 292$ K. Points correspond to $P > 20$ Torr where Ar or He is added to constant water vapor partial pressure of ~16 Torr. The intercepts yield $\gamma_0 = 0.132 \pm 0.016$ for H_2O_2 and $\gamma_0 = 0.110 \pm 0.009$ for SO_2. Diffusion parameters are discussed in the text.

consistent with a temperature-dependent H_2O_2 heterogeneous uptake rate. If the increase in H_2O_2 uptake at low pressure were due only to increasing gas-diffusion rates, then the added rare-gas points would nearly fall on top of the pure water points. The uptake rate in added Ar would be slightly lower than in pure water, reflecting the fact that gas diffusion is slightly slower in Ar than in water vapor. Conversely, the uptake rate in added He would be only slightly higher. That is the case for SO_2 uptake in added Ar, the open triangles in Figure 8, which show no significant deviation from the pure water points (solid circles), indicating there is no significant temperature dependence of the SO_2 heterogeneous uptake rate.

The following analysis attempts to quantitatively deconvolute the temperature and diffusion effects. We first analyze the high-pressure data, where there is little variation in water vapor pressure and thus droplet temperature. After determining gas-diffusion parameters from these data, we obtain heterogeneous uptake rates extrapolated to zero pressure, defined as γ_0. The temperature dependence of these uptake rates can then be interpreted in terms of the physical chemistry of the accommodation process.

Gas-Phase Diffusion. As outlined by Schwartz,[4] the gas-phase diffusion limited mass accommodation coefficient for a static single drop is given by

$$\gamma_{obsd} = \frac{1}{\frac{1}{\gamma_0} + \frac{\bar{c}d}{8D_g}} \tag{12}$$

where D_g is the gas-phase diffusion coefficient ($cm^2\ s^{-1}$). This is similar to a form derived by Fuchs and Sutugin.[27] This equation, however, is not directly applicable for diffusion near the fast-moving train of droplets employed here. For example, the observed uptake rate plotted in Figures 5 and 6 is simply proportional to droplet surface area but independent of droplet size, contrary to the prediction of eq 12.[28] However, as is clear from the half-shaded points in Figures 8 and 9, uptake is faster to droplet trains generated from the smaller 22-μm orifice.

The details of the gas mass transport probably depend on the fact that a train of droplets does not behave as the sum of single droplets. For a given orifice size, size and spacing of the droplets are not independent of one another. Our approach is to empirically fit our observations to a modified form of eq 12. If we assume there is an effective droplet diameter that is some multiple of the known orifice diameter

$$d_f = fd_o \tag{13}$$

then rearranging eq 12 gives

$$\frac{1}{\gamma_{obsd}} = \frac{P\bar{c}d_f}{8D_p} + \frac{1}{\gamma_0} \quad \text{for } D_p = D_gP \tag{14}$$

where D_p has units of atm $cm^2\ s^{-1}$. Thus, a plot of $1/\gamma_{obsd}$ versus P should be linear with a slope dependent on the diffusion parameters and an intercept corresponding to the inverse of the zero-pressure limit of the heterogeneous uptake rate.

Figure 11 plots SO_2 and H_2O_2 points from Figures 8 and 9 for $P > 20$ Torr, for which water vapor pressure was kept constant (≈16 Torr). Droplet temperature was within a degree of 292 K for all the points in Figure 11. The pressure axis is adjusted to take into account relative diffusion rates in the added He and Ar that provided the pressure variation. The pressure is expressed as an effective pressure that is a sum of the partial pressures of each constituent weighted by the binary diffusion coefficients for the trace gas in each component. For the 22-μm orifice data, the total effective pressure is normalized to that of the 61-μm data by multiplying by the ratio of the two orifice diameters to take into account the variation in the d_f factor in eq 14:

$$P_{eff} = \left\{P_{H_2O} + P_j\frac{D_{i,H_2O}}{D_{i,j}}\right\}\frac{22}{61}$$

where i and j refer to the trace gas and added rare gas, respectively. Diffusion coefficients were either taken from the literature[29] or calculated from theory.[30] The values used are listed in Table II.

TABLE II: Gas Diffusion Coefficients (atm $cm^2\ s^{-1}$)

	carrier gas		
trace gas	H_2O	Ar	He
SO_2	0.124	0.099	0.43
H_2O_2	0.243	0.22	0.61

(27) Fuchs, N. A.; Sutugin, A. G. In *Topics in Current Aerosol Research*; Hidy, G. M., Brock, J. R., Eds.; Pergamon: Oxford, 1971; p 1.

(28) For single droplets, there also should be a droplet velocity effect due to ventilation. For droplet Reynolds numbers of 0.7–8, this ventilation factor should vary from 1.1 to 1.5. No such velocity dependence is observed. See: Pruppacher, H. R.; Klett, J. D. *Microphysics of Clouds and Precipitation*; D. Reidel: Holland, 1978; p 443.

(29) Marrero, T. R.; Mason, E. A. *J. Phys. Chem. Ref. Data* **1972**, *1*, 3.

(30) Hirschfelder, J. O.; Curtiss, C. F.; Bird, R. B. *Molecular Theory of Gases and Liquids*; Wiley: New York, 1954; p 514.

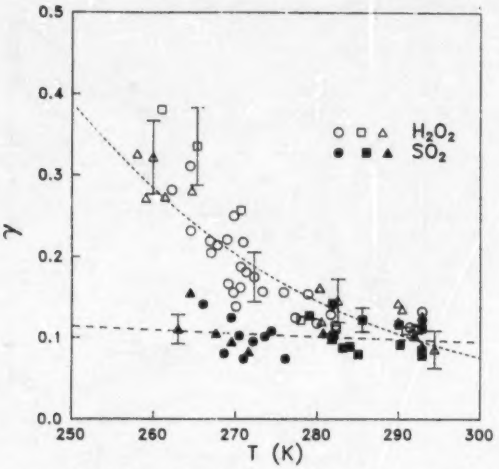

Figure 12. Plot of γ for SO_2 and H_2O_2 as a function of droplet temperature, fitting all data points for each gas to a single temperature-dependent curve. Curves were calculated from eq 21, using parameters listed in Table III. Symbol shapes match those in Figures 8–10.

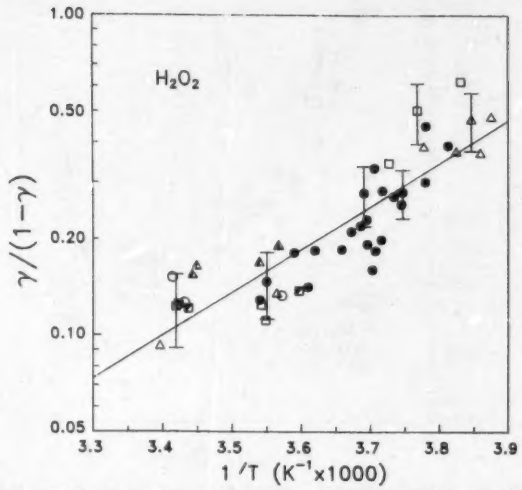

Figure 13. Semi-log plot of inverse temperature dependence for H_2O_2 accommodation coefficient (eq 21). Line is least-squares fit used to determine parameters listed in Table III. Symbols are as in Figures 9 and 10.

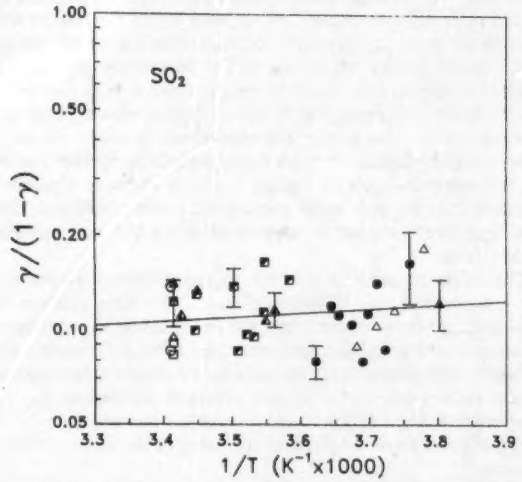

Figure 14. Semi-log plot of eq 21 for SO_2. See Figure 13. Symbols are as in Figure 8.

The plots in Figure 11 are linear within the errors over the experimental range of pressure and orifice diameter. With use of eq 13 and 14, the slopes of the SO_2 and H_2O_2 lines give the empirical orifice diameter correction $f = 2.0 \pm 0.2$ and 1.6 ± 0.3, respectively. The intercepts of the line give the zero-pressure limits, $\gamma_0 = 0.109 \pm 0.009$ and 0.132 ± 0.016 for SO_2 and H_2O_2 at 291 K. The SO_2 value was corrected from an actual intercept in Figure 11 of 0.10 to account for the SO_2 saturation at 10 ms, 10^{13} cm^{-3} and pH = 11.2.

The factor of 2 increase of these γ_0 over the γ_{obsd} values in Figures 6 and 7 represents the gas mass-transport limitation in a carrier gas composed of 15 Torr of water vapor + 4 Torr of He. The agreement between the effective droplet diameters determined for SO_2 and H_2O_2 is consistent with our knowledge of their binary diffusion coefficients in water vapor, Ar, and He. The effective droplet diameters are about the same as the actual droplet diameters.

Temperature Dependence. The broken curves in Figures 8 and 9 plot gas-diffusion-limited γ_{obsd} as a function of pressure assuming that γ_0 values obtained from Figure 11 (at 292 K) are temperature independent. The short-dashed and dashed curves assume 22- and 61-μm orifices, respectively. These curves are not exact simulations, since they assume a 95% water vapor atmosphere that does not take into account the differences in rare-gas composition of individual data points. The curves do qualitatively show the expected variation in observed uptake rate due to gas-diffusion limitations alone. The upward deviation from this line in the H_2O_2 uptake rate at low pressure reflects the apparent increase in its heterogeneous uptake rate with decreasing temperature.

The gas-diffusion limitation can be removed from γ_{obsd} by solving for γ_0 in eq 14 to give

$$\gamma_0 = \frac{1}{\frac{1}{\gamma_{obsd}} - \frac{Pcd_f}{8D_p}} \qquad (15)$$

by using the diffusion parameters in Table II and $d_f = 1.9d_o$ (determined from Figure 11).[31] The γ_0 values are then corrected according to eq 3 to give the absolute mass accommodation coefficient, γ. This correction ranged from 5% to 15% for measured γ values of 0.1–0.3.

(31) The gas-phase diffusion coefficients of Table III were assumed to have a T_g^2 dependence (*American Institute of Physics Handbook*; Gray, D. E., Ed.; McGraw-Hill: New York, 1972; pp 2-250). The temperature of the gas (T_g) was assumed to be the average of the droplet surface temperature and the ambient room temperature gas, reflecting the gas temperature and density profiles around the droplets (see the Appendix).

TABLE III: Temperature Dependence of SO_2 and H_2O_2 Uptake[a]

	γ(273 K)[a]	ΔE_{obsd},[a,b] kJ mol^{-1}	ΔE_{solv},[c] kJ mol^{-1}	A[b]	ΔS_{obsd},[a] J mol^{-1} K^{-1}	ΔS_{solv},[c] J mol^{-1} K^{-1}
SO_2	0.11 ± 0.02	-2 ± 5	-27	4×10^{-2}	25 ± 20	89
H_2O_2	0.18 ± 0.02	-26 ± 7	-55	3×10^{-6}	105 ± 18	89

[a] 2σ errors. [b] A and ΔE from eq 16. [c] Reference 37.

Figure 12 plots γ for SO_2 and H_2O_2 versus droplet temperature as calculated from the experimental water vapor pressure. Within the error bars this analysis fits all the data points to a single temperature-dependent curve for each trace gas. This is shown more clearly in Figures 13 and 14, which show semi-log plots of $\gamma/(1-\gamma)$ versus inverse temperature for H_2O_2 and SO_2, respectively. The symbols are identical with those of Figures 8 and 9. The variations observed in the uptake rate as a function of atmospheric composition and orifice size are shown to be self-consistent.

The expression $\gamma/(1-\gamma)$ is plotted in Figures 13 and 14 to account for the fact that the asymptotic value of a probability coefficient is unity (see Discussion). The slope and intercepts of the best-fit lines in Figures 13 and 14 are calculated from the relation

$$\frac{\gamma}{1-\gamma} = A \exp(-\Delta E/RT) \quad (16)$$

Values of γ (0 °C), ΔE, and A for SO_2 and H_2O_2 are listed in Table III. The errors are 2σ uncertainties, reflecting both random errors and estimation of systematic errors. Of the latter, the most significant is the correction for gas phase diffusion (eq 15), whose uncertainty is given by that of d_f. Because of the narrow temperature range, there is about a factor of 3 uncertainty in the values of A.

Discussion

For liquids with high vapor pressures ($>10^{-3}$ Torr), the dynamics of gas/liquid interactions are difficult to study because of collisions with the ambient vapor above the liquid surface. Also, the lack of symmetry or lattice structure of the liquid precludes use of techniques standard to the characterization of solid surfaces. Thus, macroscopic measurement of mass accommodation kinetics represents a practical probe of liquid surface properties.

The finite vapor pressure results in a continual flux of molecules to and from the liquid surface. Water vapor density of about 10^{17} molecules cm^{-3} corresponds to deposition and evaporation rates of about 10^7 monolayers s^{-1}, assuming unit evaporation and condensation coefficients.[9] The net imbalance between condensation to and evaporation from the droplet train, due to thermal gradients within the droplets is about 100 times smaller than the continual water vapor flux. This imbalance does not represent a significant perturbation to the water vapor exchange at the surface.

The physical effect of these fluxes depends on the time scale in question, i.e., the residence time of a trace gas molecule on the surface. For example, these fluxes are slow compared to the 10^{-12}-s interaction time of a molecular collision. On the other hand, the millisecond experimental time scale clearly cannot resolve effects due to continued water vapor evaporation/condensation. Below we discuss the relevant time scales of the gas/liquid interaction and develop a simple model that describes the accommodation process in terms of molecular interactions at the surface which can be related to the results above.

Heterogeneous Mass Transfer Kinetics. The gas/liquid mass-transfer process is a convolution of up to four processes: gas diffusion to the liquid surface, sticking and solvation or reaction at the surface, and liquid-phase diffusion away from the surface. The analysis above has attempted to deconvolute the rates of gas and liquid diffusion from the rates of mass accommodation and/or reaction within the millisecond time resolution of the experiment. A more complete analysis must consider steady-state kinetics faster than can be experimentally resolved. Following the analysis presented by Schwartz,[4,5] we start by considering the characteristic time of each step in the process. The values obtained for a given process represent the time required to establish a steady state or time-independent rate.

The characteristic gas-diffusion time to a sphere is given by

$$\tau_g = \frac{d^2}{4\pi D_g}$$

Within the droplet, the characteristic time for liquid diffusion is given by[4]

$$\tau_l = \frac{d^2}{8\pi D_l}$$

In this context, steady state is defined as a uniform concentration throughout the droplet volume. These diffusion rates are connected by τ_p, the time required for phase equilibration at the surface:

$$\tau_p = D_l\left[\frac{4HRT}{\bar{c}\gamma}\right]^2$$

This is the characteristic time for saturation of the trace gas at the liquid surface. At times longer than τ_p there will be significant reevaporation of dissolved species from the surface; the net uptake rate will be determined by the rates of liquid diffusion or reaction. Finally, if aqueous reactivity of the trace gas is important, then the reaction time is given simply by

$$\tau_{rxn} = 1/k_{rxn}$$

where k_{rxn} is the liquid-phase reaction rate. τ_{rxn} is important in the limit of low solubility, i.e., in the limit of small τ_p.

TABLE IV: Characteristic Times (second) for SO_2 and H_2O_2 Uptake into 200-μm Diameter Droplets

symbol	time	SO_2	H_2O_2
τ_g	gas diffusion	10^{-5}	10^{-5}
τ_l	liquid diffusion	10^{-1}	10^{-1}
τ_p	phase equilibrium	3×10^{-10}	1
τ_{rxn}	reaction	3×10^{-7}	

Table IV lists these characteristic times for SO_2 and H_2O_2 for a 200-μm droplet. These times need to be compared to the t_c = 1–14 ms droplet/gas contact time of the experiment. Since τ_g is shorter than t_c for both SO_2 and H_2O_2, the steady-state analysis of gas diffusion in eq 15 is justified. Minimizing τ_g is equivalent to maximizing the rate of gas diffusion; the dependence of τ_g on droplet diameter and gas-diffusion coefficient underscores the importance of using small droplets at low pressure. For both gases τ_l is longer than t_c; this indicates that the entire droplet cannot be filled with trace gas during the experiment. Only a shell 1.4–5 μm deep (calculated from eq 10) is accessed on the experimental time scale, justifying the use of eq 11 for modeling liquid-diffusion-limited uptake due to surface saturation of SO_2 at low pH.

For measuring γ, the most important characteristic time is τ_p. It indicates how large a gas/liquid concentration gradient can be maintained for the trace gas during the experiment. When τ_p is longer than t_c, the concentration gradient is large enough so that the observed uptake represents only the forward rate; i.e., γ_0 is a direct measure of γ. When τ_p is shorter than t_c, the observed uptake is due to the combination of sticking and reevaporation. In kinetic terms, the forward and reverse processes are not separated, complicating interpretation of γ_0.

τ_p is also the time that shows the largest contrast between SO_2 and H_2O_2. τ_p for H_2O_2 is 3 orders of magnitude larger than t_c, indicating there will be no surface saturation of H_2O_2 on the experimental time scale. On the other hand, τ_p for SO_2 is 6 orders of magnitude smaller than t_c, consistent with the observation of SO_2 surface saturation. The value of $\tau_p(SO_2) = 3 \times 10^{-10}$ s in Table IV represents the minimum value of τ_p, calculated for a γ of unity and the physical solubility of SO_2, $H_{SO_2} = 1.3$ M atm^{-1}. Using our measured value for $\gamma_0(SO_2) = 0.1$ and the effective ionic solubilities of $H^* = 23$ and 4200 M atm^{-1} for surface pH of 3.1 and 5.4, respectively, the resulting phase times are $\tau_p^* = 9 \times 10^{-6}$ and 0.3 s. On the millisecond scale of Figure 7, these τ_p qualitatively explain the time dependence of the lower and upper curves plotted there. These calculations show the importance of the relatively fast experimental time scale required to minimize surface saturation limitations. For the time scale of our current apparatus, $H/\gamma > 10^4$ is required for direct measurement of γ.

SO_2 Accommodation. The calculations of H^* and τ_p^* only partially describe the uptake of SO_2. These quantities describe the capacity of water to dissolve SO_2; they say nothing directly about the kinetics of the solvation process. The agreement of the curves and points in Figure 7 is an absolute measure of the $(D_l)^{1/2}H^*$ dependence in eq 11. However, $\gamma_{obsd}(t=0)$ represents the zero time limit only within the experimental time resolution. One must compare the rate of $SO_2 \rightarrow HSO_3^-$ conversion that underlies H^* to give τ_p^*. The value of $\tau_{rxn}(SO_2) = 3 \times 10^{-7}$ s in Table IV is based on the 3×10^6 s^{-1} rate for SO_2 solvation reported by Eigen et al.[32] Because τ_{rxn} is longer than τ_p, SO_2 uptake is limited by the rate of reaction that leads to the effective solubility H^*.

Because both of these characteristic times are much shorter than the millisecond experimental time scale, the observed γ_0 is

(32) Eigen, M.; Kustin, K.; Maass, G. *Z. Phys. Chem. (New Folge)* **1961**, *30*, 130.

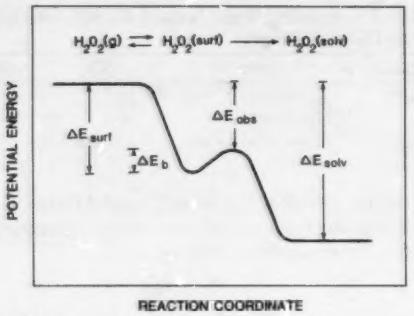

Figure 15. Schematic of reaction coordinate for physisorption and solvation of H_2O_2 on aqueous surface.

a steady-state convolution of τ_{rxn} and τ_p. Following the analysis of Schwartz and Freiberg,[5] the steady-state rate is given by[15]

$$\gamma_0 = \frac{\gamma}{1 + (\tau_{rxn}/\tau_p)^{1/2}}$$

Inserting the expressions for τ_{rxn} and τ_p

$$\gamma_0 = \frac{1}{\frac{1}{\gamma} + \frac{\bar{c}}{4HRT(D_l k_{rxn})^{1/2}}} \tag{17}$$

Inserting appropriate values for SO_2, in the limit of unit γ, the maximum observable γ_0 is predicted to be 0.03. Conversely, the measured $\gamma_0 = 0.11$ requires that $k_{rxn} = 4 \times 10^7$ s^{-1}. Depending on the actual value of γ, this k_{rxn} is at least 12 times faster than the value reported for bulk solution. This discrepancy implies that if the reported rate coefficient is correct, then the rate on the aqueous surface is faster than in the bulk solution.

This analysis is based on bulk values measured in water for SO_2 solubility, solvation kinetics, and aqueous diffusion. The measured SO_2 uptake rate is at least a factor of 3 larger than the upper limit predicted by this modeling. We have interpreted the discrepancy in terms of a surface reaction rate; actually, the discrepancy could arise from surface/bulk differences in any combination of H_{SO_2}, D_l, or k_{rxn} values. As a practical matter the point is that the measured γ_0 represents the actual heterogeneous uptake rate of SO_2 into aqueous surfaces.

Physically, this discrepancy is not surprising, since this picture of bulk processes at the liquid surface is inherently unreasonable for insoluble gases, i.e., when τ_p is short. The use of D_l to calculate τ_p implies a steady-state diffusion depth into the liquid of $(D_l\tau_p)^{1/2}$. The steady-state reaction limited uptake (eq 17) implies a diffusion depth of $(D_l/k_{rxn})^{1/2}$. For SO_2, these depths are 8 and 70 Å, respectively. The derivation of eq 17 assumes that molecular interactions in those surface layers can be separated into sticking, diffusing, and reacting steps. In the case of SO_2, the mass accommodation process intertwines heterogeneous chemical conversion and diffusion at rates significantly faster than they occur in the bulk liquid.

H_2O_2 Mass Accommodation. Temperature Dependence. The high solubility of H_2O_2 provides a very different chemical system. Indeed, the temperature dependence of H_2O_2 uptake in Figure 12 is qualitatively different than that of SO_2. The $\Delta E = -26$ kJ mol^{-1} corresponding to the slope of the line in Figure 12 indicates there is an attraction between H_2O_2 and the aqueous surface. This negative temperature dependence has been observed for adsorption of gases on solid surfaces.[7,33] This attraction has been interpreted in terms of a physisorbed state that is a precursor to the final chemisorption of the silane into the silicon surface.

Figure 15 plots a schematic of a potential energy diagram showing an attractive well corresponding to such a state for H_2O_2 accommodating on an aqueous surface. In this picture, the kinetics of H_2O_2 accommodation can be modeled in terms of competition between evaporation and solvation of physisorbed H_2O_2. We begin by assuming that thermal accommodation has unit probability; i.e., H_2O_2 is thermalized into the attractive well upon every collision with the surface. This can be justified by analogy to the unit condensation coefficient reported for H_2O molecules on water surfaces.[9] The net probability for mass accommodation is then given by the steady-state ratio of solvation and evaporation rates for physisorbed molecules leaving the attractive well:

$$\gamma = \frac{k_{solv}}{k_{evap} + k_{solv}} \tag{18}$$

We then assume that these rates can be written as simple Arrhenius rate expressions:

$$k_{evap} = B \exp(-\Delta E_{surf}/RT) \tag{19}$$

$$k_{solv} = C \exp(-\Delta E_b/RT) \tag{20}$$

where ΔE_{surf} is the depth of the attractive well and ΔE_b is the height of the barrier between the physisorbed state and the solvated state in the liquid as shown in Figure 15. On rearranging eq 18–20, we obtain

$$\frac{\gamma}{1-\gamma} = \frac{C}{B} \exp[-(\Delta E_b - \Delta E_{surf})/RT] \tag{21}$$

Equation 21 is of the same form as eq 16. Thus, ΔE of eq 16 in Figure 14 is identified as the difference between the attractive well depth and the barrier to solvation:

$$\Delta E = \Delta E_b - \Delta E_{surf}$$

The A factor of eq 16 is identified as the ratio of the preexponential factors for solvation and evaporation (C/B) from eq 19 and 20. This derivation is similar to one reported by Alnot and King[33] that was originally considered by Kisliuk.[34] Similar kinetics have also been discussed by Judeikis and Siegel in reference to surface catalysis.[35]

In this model, the measured temperature dependence of γ for H_2O_2 contains no direct information about ΔE_b or ΔE_{surf}. However, as can be seen from Figure 15, their difference $\Delta E = -26$ kJ mol^{-1} represents a significant fraction of the total solvation energy of H_2O_2, $\Delta E_{solv} = -55$ kJ mol^{-1}.

H_2O_2 and SO_2 Chemistry. In this simple picture, the preexponential factor of eq 21 (A in Table III) is a measure of the relative probability (in the absence of energetic constraints) that a molecule will enter solution as it sits in the attractive well. The small value for H_2O_2 (2×10^{-6}) implies that, even though the physisorbed H_2O_2 is relatively strongly bound, there is a very large orientation constraint limiting the penetration of H_2O_2 into the aqueous surface. In terms of transition-state theory, this corresponds to a very tightly bound transition state leading to H_2O_2 solvation. This is counter to a simple physical picture of a fluctuating, loosely bound interface at the surface of the liquid.

As listed in Table III and plotted in Figure 14, the accommodation of SO_2 has a much larger A factor, 4×10^{-2}, corresponding to the reactive uptake of SO_2 ($SO_2 \rightarrow HSO_3^-$). In this picture, the small temperature dependence ($\Delta E = -2$ kJ mol^{-1}) indicates that the height of the barrier to solvation and depth of the attractive well are about the same. Alternatively, a simpler interpretation of the SO_2 results is that SO_2 accommodation is a direct process; i.e., no physisorbed state is formed. In this picture, the A factor and ΔE of Table III are measures of the Arrhenius rate for this process.

The A factor of eq 21 can also be interpreted as a difference in the entropy of activation for accommodation and evaporation, where $A = \exp(\Delta S/R)$. These ΔS values for SO_2 and H_2O_2 accommodations are listed in Table III along with the entropy changes for SO_2 and H_2O_2 solvation. For H_2O_2, the difference in activation entropies (105 J mol^{-1} K^{-1}) is essentially the same as the overall entropy of solvation (98 J mol^{-1} K^{-1}). While

(33) Alnot, P.; King, D. A. *Surf. Sci.* **1983**, *126*, 359.

(34) Kisliuk, P. *J. Phys. Chem. Solids* **1957**, *3*, 95.

(35) Judeikis, H. S.; Siegel, S. *Atmos. Environ.* **1973**, *7*, 619.

containing no information about the conformation of H_2O_2 on the surface, this implies that the orientation constraint between the physisorbed state and the liquid is equivalent to that of H_2O_2 solvation. In the case of SO_2, the difference in activation entropies (25 J mol^{-1} K^{-1}) is only about 30% of the solvation entropy (89 J mol^{-1} K^{-1}), indicating that the rate-limiting step in SO_2 accommodation does not involve complete solvation of SO_2.

Overall, analyses based on eq 21 and the reaction coordinate of Figure 15 treat SO_2 and H_2O_2 accommodation as heterogeneous chemical reactions with no direct correlation to bulk liquid kinetics. The different solubilities of SO_2 and H_2O_2 imply different surface chemistries. These results are qualitatively different from the unit condensation coefficients reported for molecules on their own liquids.[9] One interpretation of this difference is that such condensation on pure liquids is equivalent to the first step of thermal accommodation assumed in deriving eq 21.

More detailed interpretations of these accommodation mechanisms will require more sophisticated models of the liquid surface. The possible role of the continual flux of condensing and evaporating molecules at the surface must also be considered.

Implications for Atmospheric Chemistry. The mass accommodation coefficients for both SO_2 and H_2O_2 are large enough that for typical cloud conditions, gas/liquid mass-transfer rates will not be rate limiting for the aqueous chemical processes implicated in the oxidation of S(IV).[1-5] The observation of surface saturation of SO_2 (Figure 7) directly confirms the importance of Henry's law solubility in limiting the aqueous concentrations of S(IV). More generally the detailed analysis of H_2O_2 and SO_2 mass accommodation mechanisms indicates that one must be very careful in applying bulk liquid parameters to the surface processes.

Acknowledgment. We are indebted to Dr. Frederick Kaufman for advice, encouragement, and healthy skepticism during the initial stages of this work. We deeply miss the inspiration, criticism, humor, and warm friendship his visits as an Aerodyne consultant provided. Discussions with Drs. W. Cheng and M. Martinez-Sanchez of evaporation and diffusion rates are gratefully acknowledged. This work has been supported with funding from the Electric Power Research Institute (Contract RP 2023-8) and from the Coordinating Research Council (Contract AP-8) to Aerodyne Research and by grants from the National Science Foundation (ATM-8713210) and the Environmental Protection Agency (CR812296-01-0) to Boston College.

Appendix. Droplet Temperature Equilibration

Assuming an evaporation coefficient of unity, the rate of evaporation or condensation from a spherical droplet is given by

$$\frac{dN}{dt} = \frac{\bar{c}}{4}\pi d^2[n - n_\infty]$$

where N is the number of evaporated or condensed molecules, n the vapor concentration at the droplet surface, and n_∞ the ambient vapor concentration surrounding the droplet. Assuming that temperature is equilibrated throughout the droplet, this rate can be converted to a rate of temperature change by multiplying by the ratio of the heat of vaporization (L) to the density (ρ) and heat capacity (C_v) and dividing by the droplet volume to give

$$\frac{dT}{dt} = \frac{L}{\rho C_v}\frac{\bar{c}}{4}\frac{M6}{N_A d}[n_\infty - n]$$

where M is the molecular weight of H_2O and N_A is Avogadro's number. Employing the ideal gas law and appropriate values for water

$$\frac{dT}{dt} = \frac{6 \times 10^5}{d}[P_\infty - P] \qquad \text{(A1)}$$

where P is in Torr and d in micrometers and $\bar{c}$ and P are calculated at 273 K. If one linearizes the functional dependence of P on T around P_∞

$$P = P_\infty + \left(\frac{dP}{dT}\right)_{T_\infty}[T - T_\infty]$$

then eq A1 can be solved to give a time-dependent expression for the droplet temperature:

$$T(t) = T_\infty + (T_0 - T_\infty)\exp(-\beta_s t)$$

where

$$\beta_s = \frac{6 \times 10^5}{d}\left(\frac{dP}{dT}\right)_{T_\infty}$$

and $T = T_0$ at $t = 0$. This derivation assumes that the $T^{-1/2}$ temperature dependence of $\bar{c}/RT$ in β_s is much smaller than the T dependence of the water vapor pressure. In our experiment T_0 is the temperature of liquid water passing through the orifice at $t = 0$. At 273 K, where the vapor pressure of water is 4.6 Torr

$$(dP/dT)_{273} = 0.32 \text{ Torr/K}$$

giving

$$\frac{1}{\beta_s} = \frac{d}{2 \times 10^5}$$

For a typical experimental droplet diameter of 200 μm, $1/\beta_s$ corresponds to a $1/e$ temperature equilibration time of about 1 ms. This is much shorter than the ~10-ms flight time of the droplets between the orifice and flow tube. Thus, the droplet temperature can equilibrate with the ambient water vapor on the experimental time scale.

Equation A1 assumes a cooling rate averaged over the whole droplet volume. The calculated temperature represents an upper limit to the temperature at the surface which is relevant to the experimental measurement. That temperature will depend on the evaporative cooling rate relative to the rate of thermal conduction away from the surface into the interior of the droplet. The latter can be expressed in terms of a time constant

$$\tau_d = \frac{d^2}{8\pi k_1} \qquad \text{(A2)}$$

where

$$k_1 = \frac{K_1}{\rho C_v} = 1.5 \times 10^{-3} \text{ cm}^2 \text{ s}^{-1}$$

where $K_1 = 6$ mW cm^{-1} s^{-1} K^{-1} for water. This equation is analogous to the mass diffusion time for a spherical droplet derived by Schwartz.[5] For a typical 200-μm droplet, this gives τ_d of about 10 ms.

Because this τ_d is much longer than the $1/\beta_s$ cooling time constant, one can assume that the droplet surface temperature quickly equilibrates with ambient water vapor pressure within the experimental time scale. However, because τ_d is comparable to experimental flight times, the interior volume of the droplet will not equilibrate with the surface temperature. There will be a temperature gradient within the droplet that corresponds to a continual thermal flux across the droplet surface to the ambient atmosphere. Evaluation of this flux must take into account the time-dependent thermal diffusion within the droplet.

An empirical formulation of the average droplet temperature is

$$T_{av} = T_0 - (T_\infty - T_0)[1 - (d_t/d)^3 \exp(-\beta_d t)] \qquad \text{(A3)}$$

where

$$d_t = d - (k_1 t)^{1/2}$$

$$1/\beta_d = \tau_d/3$$

At short times ($t \ll \tau_d$), this expression gives thermal diffusion into a surface shell $(k_1 t)^{1/2}$ deep. At long times ($t \geq \tau_d$), when the effective shell depth is larger than $(k_1 t)^{1/2}$, the entire droplet volume equilibrates at a rate consistent with the τ_d from eq A2. Within 10%, eq A2 is consistent with numerical evaluation of the exact infinite series solution for heat conduction into a sphere with constant surface temperature.[34] Differentiating with respect to t and multiplying by the heat capacity of the entire droplet, one obtains the corresponding time-dependent heat flux:

$$Q_d(t) = (T_\infty - T_0)\rho C_v(\pi/6)d_i^3 \exp(-\beta_d t)[(1/d_i)(k_1/t)^{1/2} + \beta_d] \quad \text{(A4)}$$

This heat flux is maintained by the latent heat released in continuous evaporation of water vapor from the droplet surface. This implies there cannot be simultaneous equilibrium of droplet surface temperature with the ambient water vapor pressure in the flow tube. Net pressure balance upon droplet switching can be achieved only by cooling the droplets slightly below T_∞ before they enter the flow tube. The droplets then initially condense water vapor to compensate for the evaporation due to the thermal flux from the interior of the droplet given in eq A4.

Because the evaporatative flux of eq A4 depends on droplet diameter, the surface temperature of different diameter droplets will not be identical. The variation in temperature can be calculated by evaluating Q_d (t = 12 ms) as the droplets enter the flow tube. $Q_d(t)$ is then integrated over the 1-ms flight time (t_c) in the flow tube. To convert this to a change in temperature, one must divide by the heat capacity of the droplet volume below the surface that is thermally accessed during t_c = 1 ms. Rearranging eq A2, the heat capacity C_s is given by

$$C_s = \frac{\pi\rho C_v}{6}[d^3 - d_i^3 \exp(-\beta_d t)] \quad \text{(A5)}$$

Assuming $Q(t)$ is constant during t_c

$$dT = Q_d t_c / C_s$$

For supercooling the droplet surface to T_∞ = 263 K from water initially at T_0 = 277 K heat fluxes Q_d (t = 12 ms) of 1.3×10^{-3} and 9×10^{-3} J s^{-1} give dT of 0.8 and 1.6 K for 140- and 270-μm droplets, respectively. Thus, for trains of 140- and 270-μm droplets the balanced pressure experiment would have average surface temperatures 0.4 and 0.8 K lower than the 263 K equilibrium temperature corresponding to the 2.1 Torr of water vapor partial pressure under these conditions.

In the coaxial apparatus, where $T_\infty - T_0 \leq 5$ °C, under typical conditions for 200-μm droplets with 4-ms flight times between the orifice and the flow tube and t_c = 10 ms in the flow tube, $dT \leq 1$ K.

For droplets cooled below room temperature, there is also a continuous heat flux between the droplets and the ambient gas, since the latter is held at room temperature at the flow tube walls. The time constant for establishing a thermal gradient around a spherical droplet is given by[4]

$$\tau_h = \frac{d^2}{8\pi k_g}$$

where

$$k_g = K_g/\rho_g C_g$$

where K_g is the thermal conductivity of water vapor. Taking 10 Torr of water vapor as a typical operating condition, $\tau_h = 10^{-6}$ s. Because this time is much less than the experimental time scale, one can assume a steady-state between droplet surface and ambient gas temperatures. The heat flux to a spherical surface at constant temperature from surrounding gas is given by[36]

$$Q_g = 2K_g d(T_\infty - T) \quad \text{(A6)}$$

For a 200-μm droplet at 263 K, this gives a flux of about 9×10^{-5} J s^{-1}. This is insignificant compared to the thermal fluxes from cooling the droplet discussed above.

More importantly, the gas-to-liquid thermal flux causes a temperature gradient in the gas above the droplet surface. This gradient is given by[36]

$$T = T_\infty - \frac{d}{2x + d}(T_\infty - T) \quad \text{(A7)}$$

where x is the distance above the surface. One measure of the temperature equilibration of ambient gas and the droplet surface is the gas temperature one mean free path from the surface. In the worst case for the data reported here, for 140-μm droplets supercooled to 263 K in a 2.3-Torr atmosphere, eq A7 predicts the gas is 2 K warmer than the droplet at one 2-μm mean free path above the surface.

Registry No. SO_2, 7446-09-5; H_2O_2, 7722-84-1.

(36) Carslaw, H. S.; Jaeger, J. C. *Conduction of Heat in Solids*; Oxford University Press: London, 1947; p 198.
(37) Wagman, D. D.; Evans, W. H.; Parker, V. B.; Schumm, R. H.; Halow, I.; Bailey, S. M.; Churney, K. L.; Nuttall, R. L. *J. Phys. Chem. Ref. Data* **1982**, *11*, Suppl. 2, 38, 56.

NOTICE

This document has been reviewed in accordance with U.S. Environmental Protection Agency policy and approved for publication. Mention of trade names or commercial products does not constitute endorsement or recommendation for use.

This article documents research that was conducted under the auspices of the U.S. Environmental Protection Agency (USEPA). As an arm of the government, the USEPA has a paid up, non-exclusive, irrevocable, worldwide license to reproduce, prepare derivative works, and distribute to the public all of the material contained herein, and to grant others acting on its behalf the right to do so. The USEPA grants to the National Technical Information Service, Department of Commerce, the right to act as its agent in the distribution of this material.